Journal of Neuroscience Methods xxx (2011) xxx–xxx

Contents lists available at ScienceDirect

Journal of Neuroscience Methods

journal homepage: www.elsevier.com/locate/jneumeth

Computerized detection and analysis of cancer chemotherapy-induced emesis in a small animal model, musk shrew

Dong Huang[a], Kelly Meyers[b], Séverine Henry[c], Fernando De la Torre[a], Charles C. Horn[b,d,e,*]

[a] Carnegie Mellon University, Robotics Institute, Pittsburgh, PA, USA
[b] University of Pittsburgh Cancer Institute, Biobehavioral Medicine in Oncology Program, Pittsburgh, PA, USA
[c] AgroSup Dijon, Dijon, France
[d] University of Pittsburgh School of Medicine, Department of Medicine: Division of Gastroenterology, Hepatology, & Nutrition/Department of Anesthesiology, Pittsburgh, PA, USA
[e] University of Pittsburgh, Center for Neuroscience, Pittsburgh, PA, USA

ARTICLE INFO

Article history:
Received 13 January 2011
Received in revised form 25 February 2011
Accepted 28 February 2011

Keywords:
Emesis
Nausea
Video tracking
Computer vision
Suncus murinus

ABSTRACT

Vomiting is a common side effect of cancer chemotherapy and many drug treatments and diseases. In animal studies, the measurement of vomiting usually requires direct observation, which is time consuming and often lacks temporal precision. Musk shrews have been used to study the neurobiology of emesis and have a rapid emetic episode (~1 s for a sequence of retching and expulsion). The aim of the current study was to develop a method to automatically detect and characterize emetic episodes induced by the cancer chemotherapy agent cisplatin. The body contour in each video frame was tracked and normalized to a parameterized shape basis. The tracked shape was projected to a feature space that maximized the shape variations in the consecutive frames during retching. The resulting one dimensional projection was sufficient to detect most emetic episodes in the acute (peak at 2 h) and delayed (peak at 54 h) phases after cisplatin treatment. Emetic episodes were relatively invariant in the number of retches (~6.2), duration (~1.2 s), inter-retch interval (~198 ms), and amplitude during the 72 h after cisplatin treatment. This approach should open a new vista into emesis research to permit tracking and analysis of emesis in a small animal model and facilitate the development of new antiemetic therapies. These results also yield a better understanding of the brain's central pattern generator for emesis and indicate that the retching response in the musk shrew (at ~5.4 Hz) is the fastest ever recorded in a free-moving animal.

1. Introduction

Vomiting and nausea often occur in patients with chronic disease, such as cancer, AIDS, and gastrointestinal disease, and can contribute to reductions in appetite, quality of life, and adherence to treatment plans that involve medicines with these side effects (Glare et al., 2004; Murakami et al., 2008; Norval, 2004). Clinically, vomiting and nausea are frequently observed with the use of cytotoxic chemotherapy agents (e.g., Ettinger et al., 2008; Hesketh, 2008). Antiemetic drugs are not always effective for controlling emesis and they can affect the efficacy of other treatments, pose potential health risks, and are expensive (Aapro, 2002; Candiotti et al., 2007; Llanes et al., 2006; Parsons et al., 2000; Sano et al., 2005; Twycross, 1994; Zhang et al., 2006a,b). Therefore, it is important to find better ways to control these side effects. However, many important aspects of the neural pathways and mechanisms for emesis are poorly understood (e.g., Horn, 2008).

In recent years, there has been an increased focus on the use of small animal models in emesis research, particularly musk shrews (*Suncus murinus*) (e.g., Horn et al., 2010b; Parker et al., 2009; Percie du Sert et al., 2010; Yamamoto et al., 2009). Notably rodents, including mice and rats, lack a vomiting response (Andrews and Horn, 2006; Andrews, 1995; Horn et al., 2010a). The musk shrew has distinct advantages as a research model, including a significant database on neuroanatomy, pharmacology, genetics, and a broad range of emetic and antiemetic drugs affecting this species (e.g., Andrews et al., 2000; Gardner et al., 1995; Hu et al., 2001, 2003, 2007; Ito et al., 1995, 2002, 2003; Ito and Seki, 1998; Matsuki et al., 1993, 1988; Mutoh et al., 1992; Okada et al., 1994; Sam et al., 2003; Torii et al., 1993, 1994, 1991; Won et al., 1998a,b). Musk shrews can be easily observed and/or videotaped for behavioral responses (Sam et al., 2003). The brain of this species is sufficiently large and well characterized to analyze nuclear groups (Andrews et al., 2000; Gill et al., 1998; Ito et al., 2002, 2003, 2005; Ito and Seki, 1998). In addition, an in situ brainstem preparation for assessing the emetic circuitry is available (Smith et al., 2002, 2001). Equally

* Corresponding author at: University of Pittsburgh Cancer Institute, Hillman Cancer Center - Research Pavilion, G.17b, 5117 Centre Avenue, Pittsburgh, PA 15213. Tel.: +1 412 623 1417; fax: +1 412 623 1119.
E-mail address: chorn@pitt.edu (C.C. Horn).

0165-0270/$ – see front matter © 2011 Elsevier B.V. All rights reserved.
doi:10.1016/j.jneumeth.2011.02.032

important is the fact that this species, slightly larger than a mouse (25–85 g), can be efficiently maintained in large numbers (in contrast to other emesis competent species like ferrets, cats, dogs and pigs) and are easily bred and handled. This convenient body size greatly facilitates routine behavioral analysis, injections, and biological sampling.

However, two significant problems exist in the measurement of emesis in musk shrews. The emetic episode in this species is extremely fast, ~1 s, compared to reports on free moving larger animals, such as ferrets (~10 s), and pigs (~7 s) (Milano et al., 1995; Percie du Sert et al., 2009a). An emetic episode is a series of retches that is usually followed by an expulsion event (a vomit) (Andrews et al., 1990). In fact, it is common for researchers using these larger species to report individual features of emetic episodes, including the number of retches and vomits (Andrews et al., 1990; King and Landauer, 1990; Simoneau et al., 2001; Thompson et al., 1992). Indeed, the number of retches might represent the major effect in some experiments (Andrews et al., 1990). Andrews et al. suggested that the retching frequency during an emetic episode could be related to the respiratory frequency, such that animals with a rapid respiration rate, like the musk shrew, might also have a more rapid retching frequency (Andrews et al., 1996). A second problem with the measurement of emesis is that it is laborious, which is not specific to the use of musk shrews. For example, in the study of cancer chemotherapy-induced emesis it is typical to measure emesis over several days. This necessitates round-the-clock video recording of animal behavior and lengthy video playback with manual coding (Percie du Sert et al., 2009b; Sam et al., 2003). Moreover, it is difficult to assess subtle patterns of vomiting that might be different with different dosages of chemotherapy or variability among musk shrews.

The goal of the current project was to find a solution to both problems using computer analysis to individually measure retches and automatically track emesis from video recordings. To accomplish this we used cisplatin (a highly emetic chemotherapy agent) to induce emesis in two experiments. In Experiment 1, we tested animals in a high contrast test chamber (dark animal on white background) for 2 h. In Experiment 2, we focused on the more challenging task of tracking emesis in the home cage (with bedding, food container, and water spout) over 3 days post-injection to capture the acute (<24 h) and delayed (>24 h) phases of cisplatin-induced emesis (see review Rudd and Andrews, 2005).

2. Materials and methods

2.1. Subjects

The subjects were 16 adult musk shrews (>162 days of age) with body weights of 56–82 g for males and 40–49 g for females. These animals were derived from breeding stock acquired from the Chinese University of Hong Kong, Prof. John Rudd (a strain originating from Taiwan). The animals were housed individually in clear plastic cages (28 cm × 17 cm × 12 cm), with a filtered air supply, using a 12-hour light/dark cycle (07:00–19:00 or 08:00–20:00 light period), and had free access to food and water. They were fed a combination of cat and mink food (mixture of 15% Purina Cat Chow Complete Formula and 25% Complete Gro-Fur mink food pellets) while in the home cage and during Experiment 2 testing (Rissman et al., 1988). At the end of each experiment, animals were euthanized by CO_2 gas from a gas cylinder. All experiments were approved by the University of Pittsburgh Institutional Animal Care and Use Committee.

2.2. Procedures for Experiments 1 (2 h) and 2 (72 h)

The doses of cisplatin are based on a prior study using 20 and 30 mg/kg cisplatin (Sam et al., 2003). In Experiment 1, at ~1100 h

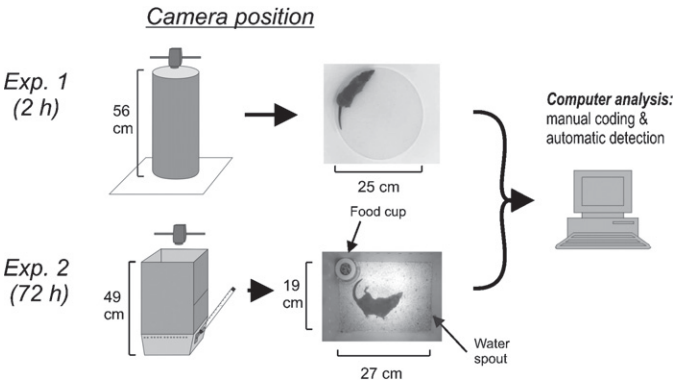

Fig. 1. Experimental chambers and camera position. In Experiment 1, the circular test chamber was positioned on top of white laboratory paper. In Experiment 2, a rectangular white acrylic enclosure was placed on top of a "home cage like" test chamber. In both experiments, the camera was positioned 61 cm above the floor of the test area.

10 animals (5 male and 5 female) were injected with cisplatin (20 mg/kg, i.p.; Sigma–Aldrich) and placed in a round chamber (Fig. 1) under an animal transfer hood and behavior was video recorded from above (Sony Handycam; DCR-SR300). Videos were stored on the internal hard drive of the camera. White lab paper was used for the bottom of the chamber to produce a high contrast with the dark coat of the musk shrew. In one animal, the camera stopped at 1 h 50 min because of power lose.

In Experiment 2, behavior of six male musk shrews was video-recorded for 72 h after injection of 30 mg/kg of cisplatin (i.p.). We used 30 mg/kg cisplatin because, unlike 20 mg/kg, this dose was reported to produce emesis in nearly all animals (Sam et al., 2003). At ~945 h an animal was placed individually into the cage (Fig. 1) within an animal transfer hood (12-hour light/dark cycle). A food cup was available and water was provided in a graduated cylinder with a sipper tube protruding into the side of the chamber (Fig. 1). Each morning at 945 h, the musk shrew was weighed and food and water containers were checked and refilled. A camera (Sony Handycam; DCR-SR300) was placed above the cage and attached to the computer via a USB port (USB 2.0 Video Capture Cable; StarTech.com). The videos were captured using Movie Maker software (Microsoft).

2.3. Manual software coding of emesis

Videos (MPEG-2) were imported into behavioral coding software (The Observer XT 10.1; Noldus Information Technology, www.noldus.com, The Netherlands). Emetic episodes were recorded manually with keystrokes by a trained observer viewing a computer monitor. An emetic episode was recognized as a sequence of contractions of the abdomen and head movements (retching). An emetic episode can occur with or without the expulsion of gastric contents (e.g., Horn et al., 2010b) and, therefore, episodes without expulsion were also counted. The Observer software allows users to slow down, reverse, and check the coding of behaviors stored in a computer file containing the codes and timestamps. To analyze the microstructure (measures from the computer algorithm, see below) of each manually labeled emetic episode we determined the video frame at the start and at the end of each event by slow motion video playback (VirtualDub; www.virtualdub.org).

2.4. Automatic detection of emesis

Given a video sequence captured at 30 frames per second of musk shrew behavior we designed a system to automatically detect emetic episodes. The system had two main components: (1) track-

Please cite this article in press as: Huang D, et al. Computerized detection and analysis of cancer chemotherapy-induced emesis in a small animal model, musk shrew. J Neurosci Methods (2011), doi:10.1016/j.jneumeth.2011.02.032

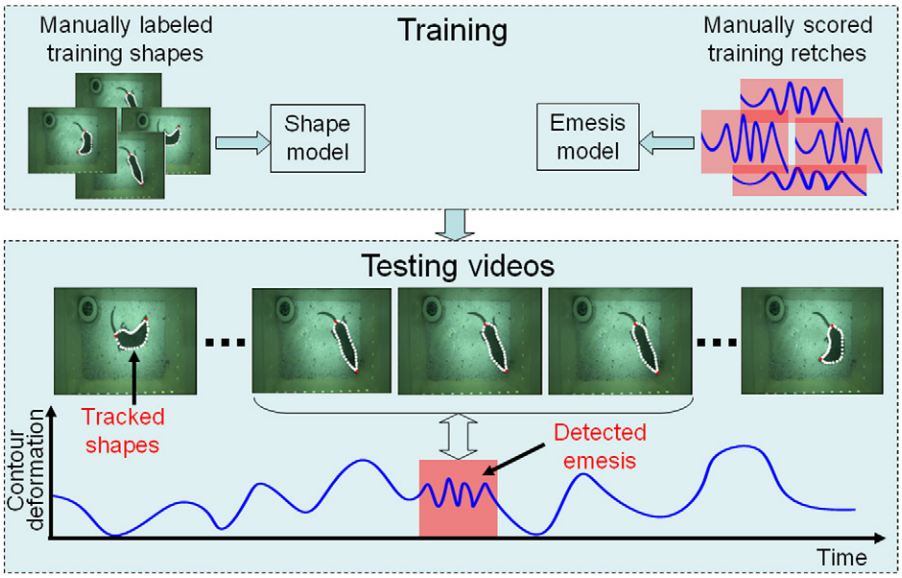

Fig. 2. Overview of the computerized detection system for emetic episodes. *Top:* Training phase to build a shape model of the body contour and a model for tracking emesis. *Bottom:* processing of video frames to detect emesis. The white outline in each frame denotes the body contour of the musk shrew. Contour deformation = maximal-retch component from the principal component analysis. See Section 2 and Appendix A for details.

ing the contour (outline) of the animal, and (2) detecting emesis from the contour. Fig. 2 provides a graphical illustration of the system.

2.4.1. Body contour tracking

Tracking the contour of the musk shrew is a challenging computer vision problem for several reasons (e.g., Branson and Belongie, 2005): (1) there are a large number of body configurations and actions that the musk shrew can perform; (2) the deformation of the shape of the body is highly non-rigid; (3) there are illumination changes, and the background is not uniform. To address these challenges, the system had two main modules: (1) pre-processing to generate the body contour in each frame, and (2) tracking the contour across frames.

2.4.1.1. Preprocessing. Given an individual video frame (denoted by **I**; Fig. 3A), the pre-processing step segments the musk shrew from the background (Fig. 3B), and extracts the animal's contour (Fig. 3C) ignoring irrelevant information such as the fur, claws, and tail. Before the musk shrew was put into the cage (for each day), we recorded a background image, i.e. $\mathbf{I}_B$. We then applied background subtraction to detect the musk shrew, i.e., the pixels containing the animal were obtained by thresholding the absolute difference between the background image $\mathbf{I}_B$ and the frame image **I**, i.e., $abs(\mathbf{I} - \mathbf{I}_B)$. However, due to the irregular illumination in the cage (e.g., brighter in the center and darker in the corners; see Fig. 1, Exp. 2 test chamber), the boundary of the animal can be corrupted when segmented with the same threshold in different cage regions. To provide robustness to non-uniform illumination we used the relative absolute difference: $\mathbf{I}_F = abs(\mathbf{I} - \mathbf{I}_B)/\mathbf{I}_B$ (Fig. 3B). Finally, the body contour (Fig. 3C) was extracted as the pixels on boundary of the segment body using morphological operators. Specifically, we subtracted the eroded version of image patch in Fig. 3B from the dilated version to get the boundary pixels (see Gonzalez and Woods, 2002 for information about morphological operators).

2.4.1.2. Contour tracking. The shape and length of the body contour can vary across video frames, as well as the number of pixels on the boundary. Therefore, the correspondence of the points on the body contours in different frames must be determined in order to model the underlying body movement across time. This was accomplished by using an extension of Point Distribution Models (PDMs) (Myronenko et al., 2006), a statistical tool to model a deformable shape template (40 landmark points were used; Fig. 4A) that defines the body contour. By matching the landmark points of the shape template (Fig. 4A) to the edge points on the body contour from each frame (Fig. 3C), the body movement can be measured as the degree of displacement between corresponding edge points matched with the same landmark points. However, we discovered that it was difficult to match the shape template to the body con-

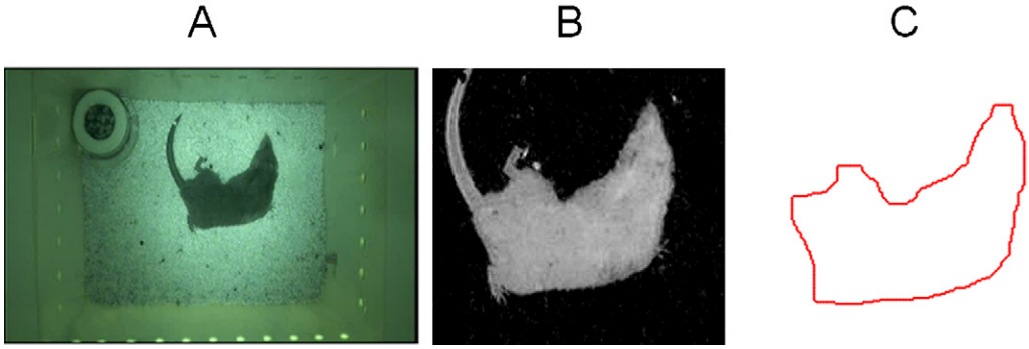

Fig. 3. Preprocessing of the video showing the (A) original image, (B) body segmentation, and (C) extraction of the musk shrew body contour.

Please cite this article in press as: Huang D, et al. Computerized detection and analysis of cancer chemotherapy-induced emesis in a small animal model, musk shrew. J Neurosci Methods (2011), doi:10.1016/j.jneumeth.2011.02.032

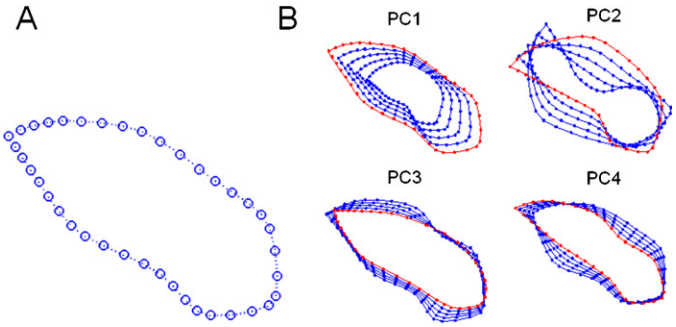

Fig. 4. Body shape template. (A) The mean of the body contour template, and (B) The superposed body contours of the shape variations (starting with the red contours) along each of the four principal components (PCs) from a principal component analysis. These modes of movement represent the most dominant variations in body shape from the training set. (For interpretation of the references to colour in this figure legend, the reader is referred to the web version of the article.)

tour in each video frame for two reasons: (1) The movements of the musk shrew are typically very fast and represent non-rigid motions, and (2) there is no reliable local shape feature or local texture feature to guarantee the correspondences between the template landmarks and the edge points of the body contour. To deal with these problems, we used an extension of PDMs, where a shape model is trained beforehand to constrain the possible deformations of the shape (see Appendix A).

Firstly, in a training phase, the statistical shape model of musk shrew body deformation was built (see Appendix A) from a set of training samples, which are the frames containing various body configuration contours of the musk shrew (see Fig. 2, top left). For each training sample, we manually labeled 40 landmarks (points) along the body contour (Fig. 4A). Ten of the 40 landmarks correspond to well-defined physical features (e.g., the nose, ears, shoulders, waist sides, thighs, and the tail end). The remaining 30 points were uniformly interpolated among those 10 landmarks. We then ran Procrustes Analysis (Dryden and Mardia, 1998) to remove rigid transformations (a rigid transformation is a change in direction, location, and scale of the animal) and compute the mean template for the body contour (Fig. 4A). Principal Component Analysis (PCA) (Jolliffe, 1986) was then performed on the aligned contours to get the dominant components that parameterize the shape model. Here, a linear combination of four dominant components (Fig. 4B) was used to approximate the shape configuration for each training video frame. Once the shape model was learned from training data, the next step was to use this model to constrain the deformation of the previously untrained video using PDMs (Fig. 5A) (see Appendix A). Finally, our algorithm deforms the shape template (the blue circles, Fig. 5A) from the initial configuration to the final state to match the edge points of the contour (the red line, Fig. 5B).

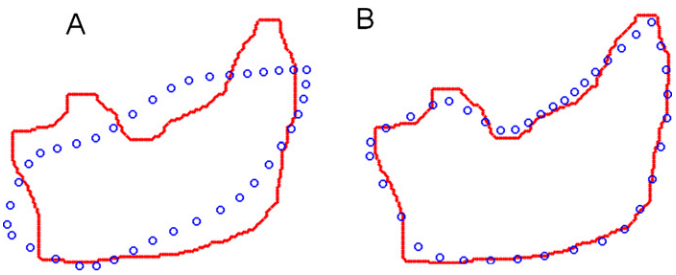

Fig. 5. Non-rigid body contour matching. The template landmarks (blue circles) are iteratively updated to match the edge points (red line) of the musk shrew from each video frame: an example of the (A) initial state before the updates and the (B) final state. (For interpretation of the references to colour in this figure legend, the reader is referred to the web version of the article.)

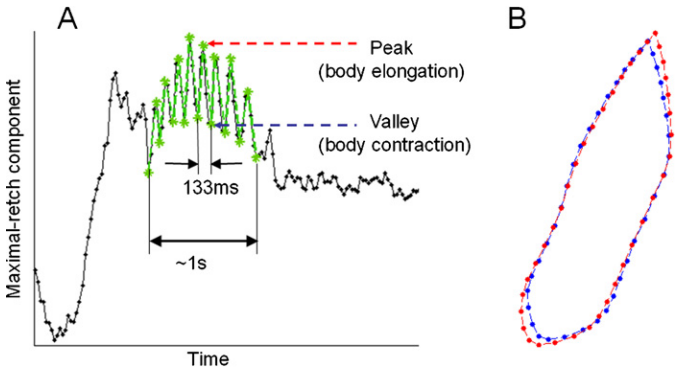

Fig. 6. Plot of the first principal component score (the maximal-retch component). (A) An example emetic episode was detected as a set of consecutive retches (~133 ms inter-retch interval with an emetic episode duration of ~1 s). (B) The blue and red contours show the body with contraction (valleys) and elongation (peaks), respectively, during a retch. (For interpretation of the references to colour in this figure legend, the reader is referred to the web version of the article.)

2.4.2. *Detection algorithm for emetic episodes*

Once the tracking was completed, each video frame was represented by a set of 40 two-dimensional landmarks (Fig. 5). The next step was to detect emetic episodes, which are characterized by the amplitude and frequency of body contour variations, i.e., a sequence of retches. However, emesis-related retches in musk shrews are very subtle movements in comparison with other common actions such as locomotion, grooming, and curling. Moreover, the amplitude and rhythm of retches vary with different animals and even for different times from the same animal. As in the previous section, we followed a learning-based approach to detect emetic episodes.

2.4.2.1. Modeling the retches during an emetic episode. In the training stage, we collected the 40 two-dimensional landmarks (i.e., an 80 dimensional vector) for all frames corresponding to emetic episodes from the five musk shrews that showed emesis in Experiment 1. We then removed the rigid transformations (rotation, location, and scale) across samples, and conducted PCA to determine the principal mode of shape changes during emetic episodes across video frames (note that this PCA is performed on the same training data used to learn the shape model). The first principal component of the PCA corresponded to the maximal shape variation during retching. We refer to this principal component as the maximal-retch component. We projected the tracked contours onto the maximal-retch component and produced a 1D representation for the original contour sequence. Fig. 6 shows the 1D sequence of the maximal-retch component.

We then computed statistics for the 1D sequence of maximal-retch component over time (across video frames), including the mean ($m_{\mathbf{d}}$) and variance ($\delta_{\mathbf{d}}$) of the displacements (d_{train}) between the peak and valley points on the 1D sequence. Here a peak (or valley) point is detected if the value on point is the higher (or lower) than its two neighboring points on the sequence. The amount of each displacement belonging to an emetic episode was computed as $\exp[-(d_{train} - m_{\mathbf{d}}/\delta_{\mathbf{d}}^2)]$. Finally, according to the training retches, the threshold for detection of an emetic event was selected as 0.7 times the standard deviation, that is $abs(d_{train} - m_{\mathbf{d}}) \leq 0.7\delta_{\mathbf{d}}$.

2.4.2.2. Detecting emesis in a test video. To detect emetic episodes in new videos (e.g., Experiment 2), we proceeded as follows: (1) detect and segment the musk shrew in each frame, (2) track the contours with a non-rigid shape matching algorithm and remove the rigid transformation, and (3) project the contours into the previously learned maximal-retch component to obtain the 1D (one dimensional) measurement sequence of the test video.

Please cite this article in press as: Huang D, et al. Computerized detection and analysis of cancer chemotherapy-induced emesis in a small animal model, musk shrew. J Neurosci Methods (2011), doi:10.1016/j.jneumeth.2011.02.032

Table 1
Computerized detection for Experiment 1 (2 h test).

	# of emetic episodes (manually scored)	Correctly detected (%)	False positives
Individual animals			
139	2	2 (100%)	0
158	5	3 (60%)	1
111	8	8 (100%)	0
196	8	8 (100%)	0
195	10	9 (90%)	1
All data			
		30 (91%)	2

At this stage, the problem of detecting emesis in the test video was reduced to detecting the retches on the 1D sequence computed above. Specifically, the peaks and valleys were detected on the 1D test sequence and the certainty of each displacement (between peaks and valleys) was computed by $\exp[-(d_{test} - m_{\mathbf{d}})^2/\delta_{\mathbf{d}}^2]$ as in the previous subsection. A candidate retch was detected when the amount of displacement exceeded the training threshold (i.e., $abs(d_{test} - m_{\mathbf{d}}) \leq 0.7\delta_{\mathbf{d}}$). Finally an emetic episode was identified when three or more consecutive retches occurred.

2.5. Data analysis

For emetic episodes, we computed standard statistics (means ± SEMs) to describe the distribution of scores. Deviations between manual and automatically scored emetic episodes were computed by percentages. Emetic episodes were analyzed for duration, the number of peaks (putative retches), inter-retch interval, signal amplitude (i.e., maximal-retch component), and retching speed (Hz).

3. Results

3.1. Manually labeled emetic episodes

3.1.1. Experiment 1 (2 h)

Cisplatin injection (20 mg/kg) produced emetic episodes (6.6 ± 1.4 events) in 5 of the 10 animals tested, three males and two females. Fig. 7A shows the mean number of emetic episodes over the 2 h test session for these five animals (Table 1, emetic episodes in each animal).

3.1.2. Experiment 2 (72 h)

Cisplatin injection (30 mg/kg) induced emesis in all six animals tested. Fig. 7B shows the mean number of emetic episodes over the 72 h test session (Table 2, emetic episodes in each animal).

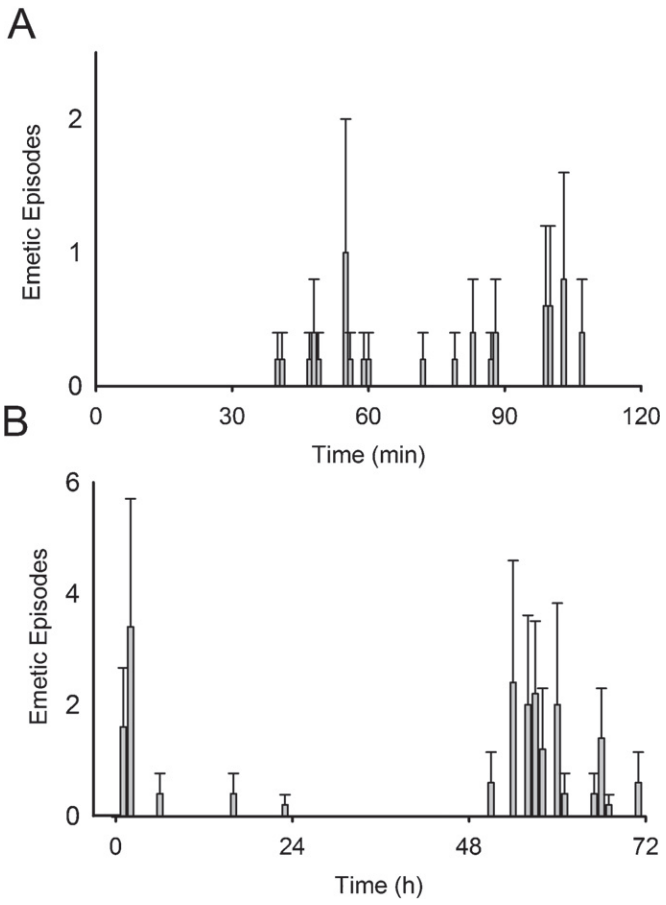

Fig. 7. Average number of emetic episodes (±SEM) induced by cisplatin in (A) each minute in Experiment 1 (20 mg/kg, i.p.; $n = 5$) and (B) each hour in Experiment 2 (30 mg/kg, i.p.; $n = 6$).

3.2. Automatic detection of emetic episodes

3.2.1. Experiment 1 (2 h)

Cisplatin injection (20 mg/kg) produced 33 emetic episodes in 5 animals and the computer algorithm successfully detected 30 of these events (91%). The three that were not detected were either of low amplitude or fewer than three consecutive retches. There were also two false positives. Table 1 shows a comparison between manual scoring and automatic detection for each animal.

3.2.2. Experiment 2 (72 h)

Cisplatin injection (30 mg/kg) produced 97 emetic episodes in 6 animals. Automatic detection of these events was most accurate during the acute phase (Day 1). Twenty-seven of 32 events were

Table 2
Computerized detection for Experiment 2 (72 h test).

	Day 1 (0–24 h)			Day 3 (48–72 h)			All Days		
	# Emetic episodes	Correct (%)	False positives	# Emetic episodes	Correct (%)	False positives	# Emetic episodes	Correct (%)	False positives
Individual animals									
189	3	3 (100%)	1	0	0	0	3	3 (100%)	1
026	0	0	0	7	6 (86%)	2	7	6 (86%)	2
110	5	5 (100%)	0	4	3 (75%)	0	9	8 (89%)	0
190	5	5 (100%)	0	5	5 (100%)	0	10	10 (100%)	0
028	0	0	0	16	14 (88%)	1	16	14 (88%)	1
152	19	14 (74%)	0	33	16 (48%)	1	52	30 (58%)	0
All data									
	32	27 (84%)	1	65	44 (68%)	4	97	71 (73%)	4

Please cite this article in press as: Huang D, et al. Computerized detection and analysis of cancer chemotherapy-induced emesis in a small animal model, musk shrew. J Neurosci Methods (2011), doi:10.1016/j.jneumeth.2011.02.032

Table 3
Computerized detection for Experiment 2 using cross-validation (72 h test).

	Day 1 (0–24 h)			Day 3 (48–72 h)			All Days		
	# Emetic episodes	Correct (%)	False positives	# Emetic episodes	Correct (%)	False positives	# Emetic episodes	Correct (%)	False positives
Individual animals									
189	3	3 (100%)	1	0	0	0	3	3 (100%)	1
026	0	0	0	7	6 (86%)	2	7	6 (86%)	2
110	5	5 (100%)	2	4	2 (50%)	0	9	7 (78%)	2
190	5	5 (100%)	0	5	5 (100%)	1	10	10 (100%)	1
028	0	0	0	16	14 (88%)	0	16	14 (88%)	0
152	19	14 (74%)	0	33	19 (58%)	1	52	33 (63%)	1
All data									
	32	27 (84%)	3	65	46 (71%)	4	97	73 (75%)	7

detected (84%) during this period with only one false positive. However, detection of events during the delayed phase (Day 3) proved more difficult with only 45 of 65 events detected (68%). This was most problematic in animal number 152, which had many more emetic episodes compared to other animals (Table 2). Events that were not detected included 8 with little lengthwise movement during retching (the basis for the maximal-retch component from PCA), 6 when the nose was against the chamber wall, 4 that displayed less than three consecutive retches, 3 that showed small amplitude retches, 2 with nose swing or curved body posture, and 1 that included an irregularly long duration single retch in a sequence. See Table 2 for a comparison of the manual and automatic scoring for each animal. Four emetic events are not included in Table 2 because these involved interference with the food cup (animal sitting on top, 2 events) or were missed in the initial manual scoring (1 manually scored event was determined to be 3 events in post hoc analyses, animal #152; see discussion section). The food cup could be easily removed and replaced with an outside food hopper in future experiments.

We also used as training data the samples from Experiment 2 and performed a leave one-out cross-validation; in other words, we ran six trials, and in each trial, data from 5 animals was used to build the model (calculating the maximal retch component and the threshold) to detect emesis and the remaining animal was used for testing. The results are included in Table 3. As can be seen in Table 3, the average results of using data from Experiment 2 is slightly better than using training data from Experiment 1. This is not surprising, because the type of emesis is more similar within datasets than between datasets. However, it is important to notice that animal 152 showed a different emetic pattern compared to the other animals, and this can bias the model when the samples from this animal are used for learning.

3.3. Analysis of the emetic episodes in Experiment 2

There was a positive correlation between the emetic episode duration and the number of retches ($r = 0.79$; Fig. 8A). Emetic episodes ranged from 3 to 12 retches (Fig. 8B), with a median of 7 and average of 6.5 ± 0.2 retches (this is calculated using all emetic episodes). Emetic episodes occurred in bouts of 1.2 ± 0.13 s with retching occurring at a speed of 5.4 ± 0.3 Hz, with an inter-retch interval of 198 ± 0.01 ms (these calculations, $n = 6$, are based on the mean of the mean values for each animal). Fig. 9 shows the duration, number of retches, inter-retch interval, mean amplitude (maximal-retch component), and speed (Hz) for the acute (24 h) and delayed (48–72 h) phases after cisplatin injection. These values represent the mean of the means of each animal, and because not all animals showed both acute and delayed phases of emesis (see Table 2) these data contain sample sizes of $n = 4$ for the acute phase and $n = 5$ for the delayed phase.

4. Discussion

These results show that it is possible to automatically detect emetic episodes and analyze the microstructure of these events from the musk shrew. Cisplatin treatment at these doses produced an emetic intensity and pattern that was consistent with other reports (e.g., Andrews et al., 2000; Horn et al., 2010b; Kwiatkowska et al., 2004; Matsuki et al., 1988; Mutoh et al., 1992; Sam et al.,

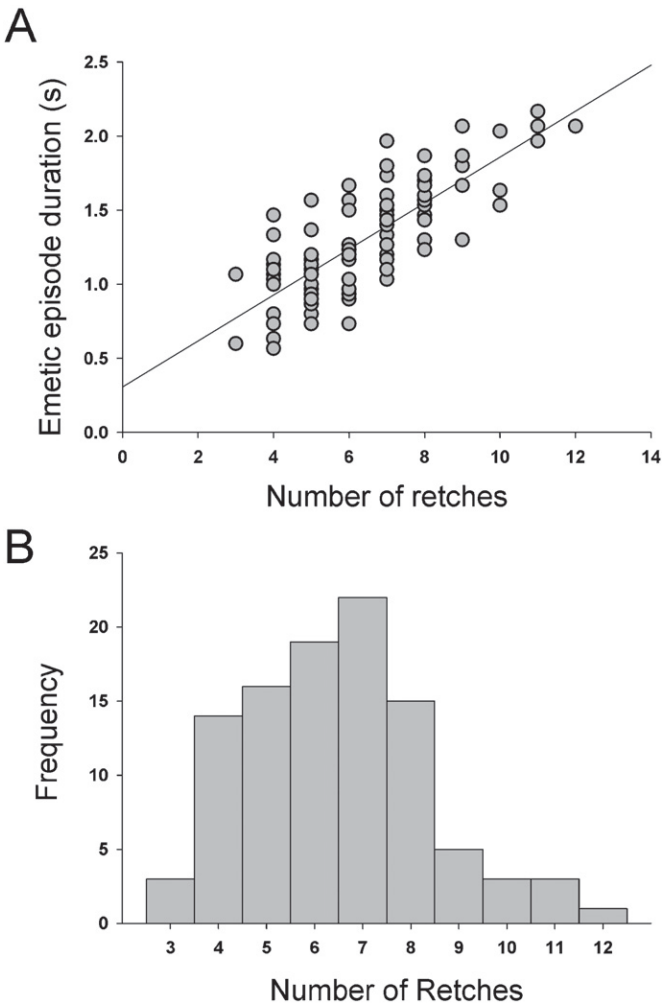

Fig. 8. Number of retches per emetic episode in Experiment 2 (72 h recording after cisplatin treatment). (A) The relationship between the number of retches and the duration of each emetic episode. (B) A frequency distribution of the number of retches in the emetic episodes. These data were computed from 6 animals and 101 emetic episodes.

Please cite this article in press as: Huang D, et al. Computerized detection and analysis of cancer chemotherapy-induced emesis in a small animal model, musk shrew. J Neurosci Methods (2011), doi:10.1016/j.jneumeth.2011.02.032

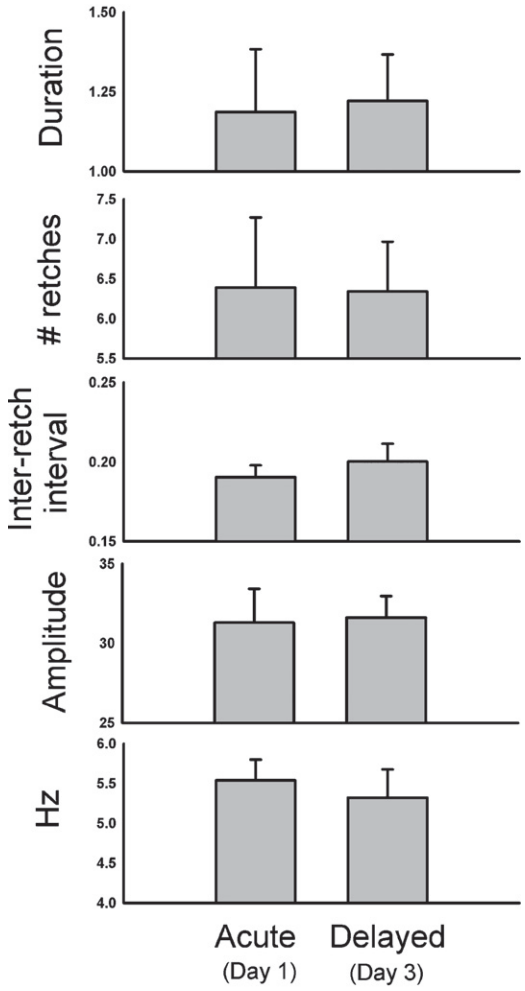

Fig. 9. Details of emetic episodes during the acute (Day 1) and delayed (Day 3) phases after cisplatin treatment. These statistics were determined by computer analysis using the maximal-retch component measure and are based on all of the manually scored emetic episodes. See Section 2 for details. Values represent mean ± SEMs (calculations are based on the mean of the mean values for each animal). These data were computed from 6 animals and 101 emetic episodes.

2003). The computer algorithm was largely successful for the detection of emetic episodes in the short-term (up to 24 h). There were 65 emetic episodes in Experiment 1 (2 h) and Experiment 2 in Day 1 (first 24 h), and 57 of these events were automatically detected with the computer algorithm (88%). However, it was more difficult to use the computer algorithm to detect events in the delayed phase, Day 3 (48–72 h), in Experiment 2; only 45 of 65 events were correctly detected (69% or 71% in cross-validation). We believe this problem is the result of subtle changes in the emetic episodes that are not present in the training set from short-term data acquired in Experiment 1. Potentially the model for detection is biased by outliers such as the intense pattern of emesis that occurred in animal 152 (Tables 2 and 3).

It would have been possible to increase the number of correctly detected events by reducing the threshold for the maximal-retch component or the criterion of at least a sequence of 3 retches. However, this would have resulted in greater number of false positives. In these experiments, there were 6 false positives in 107 detected events using the current algorithm settings (a false positive rate of 5.6%; or 9 false positives at a rate of 8.0% in 112 detections in the cross-validation). Although the main aim of this report was to explore a generic and fully automatic method to detect emetic episodes, it might be reasonable to explore a semi-automated approach in future studies. Using this approach, the threshold could be relaxed to allow greater detection and users could manually make corrections. The automatic detection results could also be improved using several strategies: round test chamber, use of more training data to build more robust estimates of the maximal-retch component, use of the second retch component from the PCA, and more accurate tracking by having a denser spatial sampling with more landmarks. A round test chamber is superior because there are no corners for the animal to poke the snout and affect the body contour. Furthermore, the food cup can be replaced with a food hopper on the outside of test chamber so that the animal will be unable to stand on an object that could also affect the body contour. However, the impact of each of these changes on the final result still needs to be determined in future research. It is also important that these detection methods are validated using different stimuli, including other drugs, motion, and conditioning effects (e.g., Matsuki et al., 1988; Parker et al., 2006; Ueno et al., 1988; Yamamoto et al., 2004).

It is important to note that manual scoring is not error free. For example, we discovered a case where the human observer scored three events as one event. We discovered these events as a result of initially looking at plots of the maximal-retch component. This led to more thorough inspection of the video and stepping the frames forward and backward one at a time. There were also isolated retches and abdominal movements that were frequently observed but were not manually scored as complete emetic episodes.

We were able to determine for the first time, using a detailed analysis of each emetic episode (made possible by computer analysis), a more complete picture of the emetic episodes in this species. These events were slightly faster (~5 vs. 4 Hz) and close to the same duration (Fig. 8) as those reported for anesthetized musk shrews (using sodium pentobarbital) in which abdominal and thoracic pressure changes were recorded during emesis induced by mechanical stimulation of the esophagus (Andrews et al., 1996). Other animals, such as ferrets, also show slower retching with anesthesia compared to the awake state (Onishi et al., 2007; Percie du Sert et al., 2009a). We also discovered that there is little to no variation in the duration, number of retches, amplitude, and inter-retch interval in the emetic episode over the course of the long-term experiment (72 h) after cisplatin treatment. This is the first time that the details of emetic episodes have been tracking over the acute and delayed phases after cisplatin treatment.

There are two major benefits to the present computerized detection approach. First, by producing a computer algorithm for emesis detection it is possible to have a high throughput analysis of emesis from video acquired during animal experiments. One significant limiting factor in the study of chemotherapy-induced emesis in animal models is that it occurs over the course of several days post treatment. Therefore, this requires very time consuming direct observation or videotaping and playback of animal behavior for multiple days (Rudd and Naylor, 1994; Sam et al., 2003). The computer algorithm used here paves the way for a substantial reduction in the time needed for data collection. Furthermore, although we use this algorithm to detect emesis in musk shrews, it should be applicable for other species, including ferrets, dogs, and cats that have a much slower retching frequency (Milano et al., 1995; Monges et al., 1978; Percie du Sert et al., 2009a) by changing the training data. Second, this algorithm permits the detailed analysis of the microstructure of emetic episodes. The emetic episode induced by cisplatin was relatively unchanged over several days post treatment (Fig. 9).

In summary, the present results represent a major advancement in this field by developing a way to detect emesis automatically using a non-invasive method to analyze video of animal behavior. Past work has focused on implantation of electrodes to record EMG or pressure changes associated with emesis (Milano et al., 1995;

Please cite this article in press as: Huang D, et al. Computerized detection and analysis of cancer chemotherapy-induced emesis in a small animal model, musk shrew. J Neurosci Methods (2011), doi:10.1016/j.jneumeth.2011.02.032

Monges et al., 1978; Percie du Sert et al., 2009a). Importantly, the current methods also allow for the first time a detailed inspection of the emetic episode from the musk shrew. This provides useful insight into the output of the central pattern generator for emesis in a free moving awake animal.

Acknowledgments

We wish to thank the University of Pittsburgh, Division of Laboratory Animal Research, especially Dawn Everard, Katie Leschak, Megan Lambert, and Dr. Joseph Newsome for excellent care of the musk shrew colony at the University of Pittsburgh Cancer Institute (UPCI). We gratefully acknowledge the funding support for this work from the UPCI (Biobehavioral Medicine in Oncology Program), and NIH grants R01DK065971 and P30 CA047904 (Cancer Center Support Grant; CCSG).

Appendix A.

The detailed algorithm for body contour tracking is described below.

A.1. Error function for non-rigid contour matching

The first step to build the error function is to learn a shape model from training data. We selected q frames as training samples with musk shrews in different configurations, and manually labeled n landmarks around the body contour (that define the shape) in each frame. Then, we ran Procrustes analysis [56] on the q samples to remove the rigid transformation (rotation, translation and scale). Let $\mathbf{Z} \in \Re^{2n\times q}$ (see the footnote[1] for the notation) be a matrix that contains the coordinates of n landmarks in each of the q aligned training shapes (after Procrustes). After removing the mean ($\bar{\mathbf{z}} = (1/n)\mathbf{Z}1$) of the aligned shapes, the non-rigid shape basis can be computed with the Singular Value Decomposition (SVD) as:

$$\mathbf{Z}\left(\mathbf{I} - \frac{1}{n}11^{\mathrm{T}}\right) \approx \mathbf{U}\boldsymbol{\Theta},$$

where $\mathbf{U} \in \Re^{2n\times k}$ contains the basis that spans the directions of maximum variation (first k eigenvectors of $\mathbf{Z}$), and $\boldsymbol{\Theta} \in \Re^{k\times 1}$ is the coefficient matrix, where each column represents the coefficient for a particular sample. We selected the k eigenvectors that preserve 95% of the energy.

Once the shape model has been learned, the next step is to match the points in the model to their corresponding edge points in a new test frame. Let $\mathbf{X} = \{\mathbf{x}_1, \cdots, \mathbf{x}_n\} \in \Re^{2\times n}$ be a matrix that contains n 2-dimensional points belonging to a shape that can be represented by the shape model (mean and columns of $\mathbf{U}$). Let $\mathbf{Y} = \{\mathbf{y}_1, \cdots, \mathbf{y}_m\} \in \Re^{2\times m}$ be a matrix that contains the m 2-dimensional edge points extracted from the frame. In the simplest case, when the two point sets $\mathbf{X}$ and $\mathbf{Y}$ mostly overlap (e.g., Fig 5B), the correspondence between a point $\mathbf{x}_i$ can be found as the closest, in Euclidean distance, of the points in $\mathbf{Y}$. However, in general given $\mathbf{Y}$ in a new test frame, we need to compute the rigid transformation and shape coefficients of the shape model, such that there is an average minimum distance between the points on $\mathbf{X}$ and $\mathbf{Y}$. To solve this problem we follow previous work by Myronenko et al. (2006).

Let us consider each point in $\mathbf{Y}$ as a center of a Gaussian-mixture model, and the points in the $\mathbf{X}$ as the samples drawn from this Gaussian-mixture model. Then, the optimal point set $\mathbf{X}$ that maximizes its likelihood with points in $\mathbf{Y}$ will provide the matching or correspondence, and it can be solved by minimizing the following energy function (Myronenko et al., 2006),

$$E(\mathbf{X}) = -\sum_{j=1}^{m}\log\sum_{i=1}^{n}\exp\left\{-\frac{1}{2\delta}\left\|\mathbf{y}_j - \mathbf{x}_i\right\|_2^2\right\}$$

where δ is a bandwidth parameter.

At this point recall that the feasible configuration for $\mathbf{X}$ is a linear combination of the (mean $\bar{\mathbf{Z}}$ and columns of $\mathbf{U}$) plus a rigid transformation (rotation, scale and translation).

Following previous work (Fitzgibbon, 2003; Myronenko et al., 2006; Zhang, 1994), we use the following optimization strategy for $E(\mathbf{X})$: at the 0th iteration, $\mathbf{X}^0 = \bar{\mathbf{Z}}$ ($\bar{\mathbf{Z}} \in \Re^{2\times n}$ is a rearrangement of the mean vector $\bar{\mathbf{z}} \in \Re^{2n\times 1}$), that is $\mathbf{X}^0$, is the mean of the shape model. Then, we iteratively update $\mathbf{X}$ as $\mathbf{X}^{t+1} = s^t\mathbf{R}^t\mathbf{X}^t + \mathbf{V}^t$ while optimizing for the rigid and non-rigid transformation parameters. t denotes the iteration step, s^t is the scaling factor, $\mathbf{R}^t \in \Re^{2\times 2}$ is the rotation matrix, and $\mathbf{V}^t \in \Re^{2\times n}$ contains the displacement. Optimization of $E(\mathbf{X})$ to find the optimal $\mathbf{X}$ that matches the points in $\mathbf{Y}$ and constraint $\mathbf{X}^t$ can be rewritten as the follows:

$$E(\mathbf{X}^t, \delta^t, s^t, \mathbf{R}^t, \mathbf{V}^t) = -\sum_{j=1}^{m}\log\sum_{i=1}^{n}\exp\left\{-\frac{1}{2\delta^t}\left\|\mathbf{y}_j - (s^t\boldsymbol{R}^t\boldsymbol{x}_i^t + \boldsymbol{v}_i^t)\right\|_2^2\right\} + \frac{\lambda}{2}\left\|\mathbf{V}^t\left(\mathbf{I} - \frac{1}{n}11^{\mathrm{T}}\right) - \mathbf{V}^*(\mathbf{U})\right\|_F^2,$$

where $\mathbf{v}_i{}^t \in \Re^{2\times 1}$ is the ith column of $\mathbf{V}^t \in \Re^{2\times n}$, $\mathbf{V}^*(\mathbf{U}) \in \Re^{2\times n}$ contains the non-rigid part of the displacement $\mathbf{V}^t$ that can be reconstructed by the pre-learned shape basis $\mathbf{U} \in \Re^{2n\times k}$. The first term of the error function $E(\mathbf{X}^t, \delta^t, s^t, \mathbf{R}^t, \mathbf{V}^t)$ measures the similarity between $\mathbf{X}^t$ and $\mathbf{Y}$, while the second term constrains the deviations of $\mathbf{X}^t$ from the pre-learned shape model (mean $\bar{\mathbf{Z}}$ and columns of $\mathbf{U}$). The second term encourages solutions of $\mathbf{X}^t$ such that the displacement $\mathbf{V}^t$ is close to the subspace generated by model (mean $\bar{\mathbf{Z}}$ and columns of $\mathbf{U}$).

To do this, the second term minimizes the difference between the non-rigid part of $\mathbf{V}^t$ and $\mathbf{V}^*(\mathbf{U})$, i.e. $\left\|\mathbf{V}^t(\mathbf{I} - (1/n)11^{\mathrm{T}}) - \mathbf{V}^*(\mathbf{U})\right\|_F^2$, where $(1/n)\mathbf{V}^t11^{\mathrm{T}}$ denotes the rigid part of the displacement, i.e. translation. The mathematical description of $\mathbf{V}^*(\mathbf{U})$ is given below.

A.2. Optimization algorithm

This subsection describes the optimization algorithm for minimizing $E(\mathbf{X}^t, \delta^t, s^t, \mathbf{R}^t, \mathbf{V}^t)$ with respect to the parameters (δ^t, s^t, $\mathbf{R}^t$, $\mathbf{V}^t$) and the shape $\mathbf{X}^t$.

Following previous work (Myronenko et al., 2006), we transformed the problem of minimizing $E(\delta^t, s^t, \mathbf{R}^t, \mathbf{V}^t)$ to minimization of its upper bound:

$$Q(\mathbf{X}^t, \delta^t, s^t, \mathbf{R}^t, \mathbf{V}^t) = \frac{1}{2\delta^t}\sum_{j=1}^{m}\sum_{i=1}^{n}p\left(\boldsymbol{x}_i\left|\mathbf{y}_j\right.\right)\left\|\mathbf{y}_j - (s^t\boldsymbol{R}^t\boldsymbol{x}_i{}^t + \boldsymbol{v}_i)\right\|_2^2 + \frac{md}{2}\log\delta^t + \frac{\lambda}{2}\left\|\mathbf{V}^t\mathbf{H} - \mathbf{V}^*(\mathbf{U})\right\|_F^2,$$

where $p\left(\boldsymbol{x}_i\left|\mathbf{y}_j\right.\right)$ is the posterior probability of the ith point in $\mathbf{X}^t$ belonging to the local Gaussian model centered at the jth edge point in $\mathbf{Y}$, and $\mathbf{H} = \left(\mathbf{I} - \frac{1}{n}11^{\mathrm{T}}\right)$.

To optimize $Q(\mathbf{X}^t, \delta^t, s^t, \mathbf{R}^t, \mathbf{V}^t)$ we used an Expectation-Maximization (EM) type algorithm that alternates between two steps:

[1] Bold capital letters denote matrices $\mathbf{X}$, bold lower-case letters a column vector $\mathbf{x}$. $\mathbf{x}_j$ represents the jth column of the matrix $\mathbf{X}$. Vector $\mathbf{1}$ is the vector of all ones. All non-bold letters represent scalar variables. x_{ij} denotes the scalar in the row i and column j of the matrix $\mathbf{X}$ and the scalar ith element of a column vector x_j. $\|\mathbf{x}\|_2^2$ denotes the norm of the vector $\mathbf{x}$. $tr(\mathbf{A}) = \sum_i a_{ii}$ is the trace of the matrix $\mathbf{A}$ and $diag(\mathbf{a})$ denotes a operator that generates a diagonal matrix with the elements of the vector a. $||\mathbf{A}||_F^2 = tr(\mathbf{A}^{\mathrm{T}}\mathbf{A}) = tr(\mathbf{A}\mathbf{A}^{\mathrm{T}})$ designates the Frobenious norm of matrix $\mathbf{A}$.

Given the initial guess of parameters as

$$\mathbf{X}^0 = \bar{\mathbf{Z}},\ s^0 = 1,\ \mathbf{R}^0 = \mathbf{I},\ \mathbf{V}^0 = 0,$$
$$\delta^0 = \frac{1}{nmd}\sum_{j=1}^{m}\sum_{i=1}^{n}\left\|\mathbf{y}_j - \mathbf{x}_i{}^0\right\|_2^2.$$

The E-step: At the *i*th iteration, the posterior probability of $\boldsymbol{x}_i$ matching $\boldsymbol{y}_j$ is

$$p\left(\boldsymbol{x}_i \left| \boldsymbol{y}_j\right.\right) = \frac{\exp\left\{-\left\|\boldsymbol{y}_j - (s^t\mathbf{R}^t\mathbf{x}_i{}^t + \mathbf{v}_i{}^t)\right\|_2^2/2\delta^t\right\}}{\sum_{q=1}^{n}\exp\left\{-\left\|\boldsymbol{y}_j - (s^t\mathbf{R}^t\mathbf{x}_i{}^t + \mathbf{v}_i{}^t)\right\|_2^2/2\delta^t\right\} + \varepsilon},$$

where $\varepsilon = (2\pi\delta^t)^{d/2}(\gamma/1-\gamma)(n/m)$ accounts for outliers. $\gamma \in [0, 1]$ controls the level of robustness.

The M-step: At the *i*th iteration, the m-step computes the scale s^t, rotation $\mathbf{R}^t$ and the displacement $\mathbf{V}^t$, then updates $\mathbf{X}^t$ to get the new version of the shape as $\mathbf{X}^{t+1} = s^t\mathbf{R}^t\mathbf{X}^t + \mathbf{V}^t$. At last, the Gaussian parameter δ^t is updated based on $\mathbf{X}^{t+1}$.

Let matrix $\mathbf{P} \in \Re^{n\times m}$ contains the elements $P_{ij} = p\left(\boldsymbol{x}_i \left| \boldsymbol{y}_j\right.\right)$ ($i = 1, \ldots, n$; $j = 1, \ldots, m$), then the scale s^t and rotation $\mathbf{R}^t$ can be computed using the method in Myronenko et al. (2006) as follows:

- *Compute* $\boldsymbol{\mu}_{\mathbf{X}} = \frac{1}{1^{\mathrm{T}}\mathbf{P}1}(\mathbf{X}^t)^{\mathrm{T}}\mathbf{P}^{\mathrm{T}}1$, $\quad \boldsymbol{\mu}_{\mathbf{Y}} = \frac{1}{1^{\mathrm{T}}\mathbf{P}1}\mathbf{Y}^{\mathrm{T}}\mathbf{P}^{\mathrm{T}}1$;
- *Compute* $\hat{\mathbf{X}}^t = \mathbf{X}^t - \boldsymbol{\mu}_{\mathbf{X}}1^{\mathrm{T}}$, $\quad \hat{\mathbf{Y}}^t = \mathbf{Y} - \boldsymbol{\mu}_Y 1^{\mathrm{T}}$;
- Perform SVD of $\mathbf{A} = \mathbf{USV}^{\mathrm{T}}$ where $\mathbf{A} = \hat{\boldsymbol{X}}^t\mathbf{P}(\hat{\mathbf{Y}}^t)^{\mathrm{T}}$,
- $\mathbf{R}^t = \mathbf{UCV}^{\mathrm{T}}$ where $\mathbf{C} = \mathrm{diag}(1, \ldots 1, \det(\mathbf{UV}^{\mathrm{T}}))$,
- $s^t = \frac{tr(\mathbf{R}^t\mathbf{A})}{tr[\hat{\mathbf{X}}^t diag(\mathbf{P}1)(\hat{\mathbf{X}}^t)^{\mathrm{T}}]}$.

Before computing the displacement $\mathbf{V}^t \in \Re^{2\times n}$ that minimizes $Q(\mathbf{X}^t, \delta^t, s^t, \mathbf{R}^t, \mathbf{V}^t)$, $\mathbf{V}^*(\mathbf{U}) \in \Re^{2\times n}$ is computed using the basis of the model $\mathbf{U} \in \Re^{2n\times k}$ using the following method.

First, let $\tilde{\mathbf{V}}^t$ be the preliminary version of displacement that matches $s^t\mathbf{R}^t\mathbf{X}^t$ to $\mathbf{Y}$, and $\tilde{\mathbf{V}}^t$ can be computed by taking the derivative, $\partial Q/\partial \mathbf{V}^t$, and making it equal to zero when $\lambda = 0$,

$$\tilde{\mathbf{V}}^t = (\mathbf{YP}^{\mathrm{T}} - \mathbf{X}^t\, diag\{\mathbf{P}1\})(diag\{\mathbf{P}1\})^{-1}$$

Since $\tilde{\mathbf{V}}^t$ is in the 2-D image space, it needs to be transformed to the $2n$ dimensional space of the shape model before computing its reconstructed version $\mathbf{V}^*(\mathbf{U})$ using the basis $\mathbf{U}$ of the shape model. Note this transformation, denoted by a function $\mathbf{w}(\cdot)$, contains the same operations (scaling and rotation) that align $s^t\mathbf{R}^t\mathbf{X}^t$ is to the mean training shape $\bar{\mathbf{z}} \in \Re^{2n\times 1}$ to get the $2n$ dimensional concatenated vector $\tilde{\mathbf{x}}^t = \mathbf{w}(s^t\mathbf{R}^t\mathbf{X}^t) \in \Re^{2n\times 1}$. We get the preliminary displacement in the $2n$-D space of shape model as $\tilde{\mathbf{v}}^t = \mathbf{w}(\tilde{\mathbf{V}}^t) \in \Re^{2n\times 1}$. Then, the $2n$ dimensional vector reconstructed by the pre-learned shape model is computed as $\tilde{\mathbf{v}}^*(\mathbf{U}) = \mathbf{UU}^{\mathrm{T}}\tilde{\mathbf{v}}^t \in \Re^{2n\times 1}$. Transforming back to the image space, we have $\mathbf{V}^*(\mathbf{U}) = \mathbf{W}^{-1}(\tilde{\mathbf{v}}^*(\mathbf{U})) \in \Re^{2\times n}$, where $\mathbf{W}^{-1}(\cdot)$ is inverse function of $\mathbf{w}(\cdot)$.

After $\mathbf{V}^*(\mathbf{U})$ is computed, taking partial derivatives of Q with respect to $\mathbf{V}^t$, we obtain the optimal displacement

$$\mathbf{V}^t = (\mathbf{YP}^{\mathrm{T}} - \mathbf{X}^t\, diag\{\mathbf{P}1\} + \lambda\delta^t\mathbf{V}^*(\mathbf{U})\mathbf{H})(diag\{\mathbf{P}1\} + \lambda\delta^t\mathbf{H}^2)^{-1}$$

After computing s^t, $\mathbf{R}^t$, $\mathbf{V}^t$, the shape $\mathbf{X}^t$ is updated as $\mathbf{X}^{t+1} = s^t\mathbf{R}^t\mathbf{X}^t + \mathbf{V}^t$.

Given the new shape $\mathbf{X}^{t+1}$, the Gaussian parameter δ^t is updated as:

$$\delta^{t+1} = \frac{1}{md}\sum_{j=1}^{m}\sum_{i=1}^{n}p\left(\mathbf{x}_i \left| \mathbf{y}_j\right.\right)\left\|\mathbf{y}_j - \mathbf{x}_i{}^{t+1}\right\|_2^2 = \frac{1}{md}[tr(\mathbf{Y}diag\{\mathbf{P}^{\mathrm{T}}1\}\mathbf{Y}^{\mathrm{T}}) - 2tr(\mathbf{X}^{t+1}\mathbf{PY}^T) + tr(\mathbf{X}^{t+1}diag\{\mathbf{P}1\}(\mathbf{X}^{t+1})^{\mathrm{T}})]$$

The above E-step and M-step are alternated until the change of $\mathbf{V}^t$ is small. After convergence, the subset of edge points in $\mathbf{Y}$ that corresponds (is nearest) to the points in $\mathbf{X}^t$ is used to represent the matched contour in the new testing image.

References

Aapro MS. How do we manage patients with refractory or breakthrough emesis? Support Care Cancer 2002;10:106–9.
Andrews P, Torii Y, Saito H, Matsuki N. The pharmacology of the emetic response to upper gastrointestinal tract stimulation in *Suncus murinus*. Eur J Pharmacol 1996;307:305–13.
Andrews PL, Horn CC. Signals for nausea and emesis: implications for models of upper gastrointestinal diseases. Auton Neurosci 2006;125:100–15.
Andrews PL, Okada F, Woods AJ, Hagiwara H, Kakaimoto S, Toyoda M, et al. The emetic and anti-emetic effects of the capsaicin analogue resiniferatoxin in *Suncus murinus*, the house musk shrew. Br J Pharmacol 2000;130:1247–54.
Andrews PLR. Why do some animals lack a vomiting reflex? Physiol Zool 1995;68:61.
Andrews PLR, Bhandari P, Garland S, Bingham S, Davis CJ, Hawthorn J, et al. Does retching have a function? An experimental study in the ferret. Pharmacodyn Therapeut 1990;9:135–52.
Branson K, Belongie S. Tracking multiple mouse contours (without too many samples). In: IEEE Conference on Computer Vision and Pattern Recognition; 2005.
Candiotti KA, Nhuch F, Kamat A, Deepika K, Arheart KL, Birnbach DJ, et al. Granisetron versus ondansetron treatment for breakthrough postoperative nausea and vomiting after prophylactic ondansetron failure: a pilot study. Anesth Analg 2007;104:1370–3, table.
Dryden IL, Mardia KV. Statistical shape analysis. Chichester; New York: John Wiley & Sons; 1998.
Ettinger DS, Armstrong DK, Barbour S, Berger MJ, Bierman PJ, Bradbury B, et al. NCCN clinical practice guidelines in oncology: antiemesis. National Comprehensive Cancer Network; 2008.
Fitzgibbon A. Robust registration of 2D and 3D point sets. Image Vision Comput 2003;21:1145–53.
Gardner CJ, Twissell DJ, Dale TJ, Gale JD, Jordan CC, Kilpatrick GJ, et al. The broad-spectrum anti-emetic activity of the novel non-peptide tachykinin NK1 receptor antagonist GR203040. Br J Pharmacol 1995;116:3158–63.
Gill CJ, Wersinger SR, Veney SL, Rissman EF. Induction of fos-like immunoreactivity in musk shrews after mating. Brain Res 1998;811:21–8.
Glare P, Pereira G, Kristjanson LJ, Stockler M, Tattersall M. Systematic review of the efficacy of antiemetics in the treatment of nausea in patients with far-advanced cancer. Support Care Cancer 2004;12:432–40.
Gonzalez RC, Woods RE. Digital image processing. 2nd ed. Upper Saddle River, NJ: Prentice Hall; 2002.
Hesketh PJ. Chemotherapy-induced nausea and vomiting. N Engl J Med 2008;358:2482–94.
Horn CC. Why is the neurobiology of nausea and vomiting so important? Appetite 2008;50:430–4.
Horn CC, Kimball BA, Gathright GR, Yates BJ, Andrews PLR. Why don't rats and mice vomit? A behavioral and anatomical investigation. Pittsburgh, PA, USA: Society for the Study of Ingestive Behavior; 2010a.
Horn CC, Still L, Fitzgerald C, Friedman MI. Food restriction, refeeding, and gastric fill fail to affect emesis in musk shrews. Am J Physiol Gastrointest Liver Physiol 2010b;298:G25–30.
Hu DL, Omoe K, Saleh MH, Ono K, Sugii S, Nakane A, et al. Analysis of the epitopes on staphylococcal enterotoxin A responsible for emetic activity. J Vet Med Sci 2001;63:237–41.
Hu DL, Omoe K, Shimoda Y, Nakane A, Shinagawa K. Induction of emetic response to staphylococcal enterotoxins in the house musk shrew (*Suncus murinus*). Infect Immun 2003;71:567–70.
Hu DL, Zhu G, Mori F, Omoe K, Okada M, Wakabayashi K, et al. Staphylococcal enterotoxin induces emesis through increasing serotonin release in intestine and it is downregulated by cannabinoid receptor 1. Cell Microbiol 2007;9:2267–77.
Ito C, Isobe Y, Kijima H, Kiuchi Y, Ohtsuki H, Kawamura R, et al. The anti-emetic activity of GK-128 in *Suncus murinus*. Eur J Pharmacol 1995;285:37–43.
Ito H, Nishibayashi M, Kawabata K, Maeda S, Seki M, Ebukuro S. Immunohistochemical demonstration of c-fos protein in neurons of the medulla oblongata of the musk shrew (*Suncus murinus*) after veratrine administration. Exp Anim 2002;51:19–25.
Ito H, Nishibayashi M, Kawabata K, Maeda S, Seki M, Ebukuro S. Induction of Fos protein in neurons in the medulla oblongata after motion- and X-

Please cite this article in press as: Huang D, et al. Computerized detection and analysis of cancer chemotherapy-induced emesis in a small animal model, musk shrew. J Neurosci Methods (2011), doi:10.1016/j.jneumeth.2011.02.032

irradiation-induced emesis in musk shrews (*Suncus murinus*). Auton Neurosci 2003;107:1–8.
Ito H, Nishibayashi M, Maeda S, Seki M, Ebukuro S. Emetic responses and neural activity in young musk shrews during the breast-feeding/weaning period: comparison between the high and low emetic response strains using a shaking stimulus. Exp Anim 2005;54:301–7.
Ito H, Seki M. Ascending projections from the area postrema and the nucleus of the solitary tract of *Suncus murinus*: anterograde tracing study using Phaseolus vulgaris leucoagglutinin. Okajimas Folia Anat Jpn 1998;75:9–31.
Jolliffe IT. Principal component analysis. New York: Springer-Verlag; 1986.
King GL, Landauer MR. Effects of zacopride and BMY25801 (batanopride) on radiation-induced emesis and locomotor behavior in the ferret. J Pharmacol Exp Ther 1990;253:1026–33.
Kwiatkowska M, Parker LA, Burton P, Mechoulam R. A comparative analysis of the potential of cannabinoids and ondansetron to suppress cisplatin-induced emesis in the *Suncus murinus* (house musk shrew). Psychopharmacology (Berl) 2004;174:254–9.
Llanes LR, Fassbender K, Baracos VE, Watanabe S. Drug utilization review on a tertiary palliative care unit. J Pain Symptom Manage 2006;31:457–64.
Matsuki N, Torii Y, Saito H. Effects of iron and deferoxamine on cisplatin-induced emesis: further evidence for the role of free radicals. Eur J Pharmacol 1993;248:329–31.
Matsuki N, Ueno S, Kaji T, Ishihara A, Wang CH, Saito H. Emesis induced by cancer chemotherapeutic agents in the *Suncus murinus*: a new experimental model. Jpn J Pharmacol 1988;48:303–6.
Milano S, Blower P, Romain D, Grelot L. The piglet as a suitable animal model for studying the delayed phase of cisplatin-induced emesis. J Pharmacol Exp Ther 1995;274:951–61.
Monges H, Salducci J, Naudy B. Dissociation between the electrical activity of the diaphragmatic dome and crura muscular fibers during esophageal distension, vomiting and eructation An electromyographic study in the dog. J Physiol (Paris) 1978;74:541–54.
Murakami N, Nakagawa K, Yamashita H, Nagawa H. Palliative radiation therapy for advanced gastrointestinal cancer. Digestion 2008;77(Suppl. 1):29–35.
Mutoh M, Imanishi H, Torii Y, Tamura M, Saito H, Matsuki N. Cisplatin-induced emesis in *Suncus murinus*. Jpn J Pharmacol 1992;58:321–4.
Myronenko A, Song X, Carreira-perpiñán Á. Non-rigid point set registration: coherent point drift. Adv Neural Inform Process Syst 2006.
Norval DA. Symptoms and sites of pain experienced by AIDS patients. S Afr Med J 2004;94:450–4.
Okada F, Torii Y, Saito H, Matsuki N. Antiemetic effects of serotonergic 5-HT1A-receptor agonists in *Suncus murinus*. Jpn J Pharmacol 1994;64:109–14.
Onishi T, Mori T, Yanagihara M, Furukawa N, Fukuda H. Similarities of the neuronal circuit for the induction of fictive vomiting between ferrets and dogs. Auton Neurosci 2007;136:20–30.
Parker LA, Kwiatkowska M, Mechoulam R. Delta-9-tetrahydrocannabinol and cannabidiol, but not ondansetron, interfere with conditioned retching reactions elicited by a lithium-paired context in *Suncus murinus*: an animal model of anticipatory nausea and vomiting. Physiol Behav 2006;87:66–71.
Parker LA, Limebeer CL, Rock EM, Litt DL, Kwiatkowska M, Piomelli D. The FAAH inhibitor URB-597 interferes with cisplatin- and nicotine-induced vomiting in the *Suncus murinus* (house musk shrew). Physiol Behav 2009;97:121–4.
Parsons SK, Hoorntje LE, Levine KJ, Mayer DK, Eichelberger WJ, Guinan EC. Balancing efficacy with cost: antiemetic control in the pediatric stem cell transplant (SCT) population. Bone Marrow Transplant 2000;25:553–7.
Percie du Sert N, Chu KM, Wai MK, Rudd JA, Andrews PL. Reduced normogastric electrical activity associated with emesis: a telemetric study in ferrets. World J Gastroenterol 2009a;15:6034–43.
Percie du Sert N, Chu KM, Wai MK, Rudd JA, Andrews PL. Telemetry in a motion-sickness model implicates the abdominal vagus in motion-induced gastric dysrhythmia. Exp Physiol 2010;95:768–73.
Percie du Sert N, Rudd JA, Moss R, Andrews PL. The delayed phase of cisplatin-induced emesis is mediated by the area postrema and not the abdominal visceral innervation in the ferret. Neurosci Lett 2009b;465:16–20.
Rissman EF, Silveira J, Bronson FH. Patterns of sexual receptivity in the female musk shrew (*Suncus murinus*). Horm Behav 1988;22:186–93.
Rudd JA, Andrews PLR. Mechanisms of acute, delayed, and anticipatory emesis induced by anticancer therapies. In: Hesketh PJ, editor. Management of nausea and vomiting in cancer and cancer treatment. Sudbury, MA: Jones and Bartlett; 2005. p. 15–65.
Rudd JA, Naylor RJ. Effects of 5-HT3 receptor antagonists on models of acute and delayed emesis induced by cisplatin in the ferret. Neuropharmacology 1994;33:1607–8.
Sam TS, Cheng JT, Johnston KD, Kan KK, Ngan MP, Rudd JA, et al. Action of 5-HT3 receptor antagonists and dexamethasone to modify cisplatin-induced emesis in *Suncus murinus* (house musk shrew). Eur J Pharmacol 2003;472:135–45.
Sano HS, Waddell JA, Solimando Jr DA, Doulaveris P, Myhand R. Study of the effect of standardized chemotherapy order forms on prescribing errors and anti-emetic cost. J Oncol Pharm Pract 2005;11:21–30.
Simoneau II, Hamza MS, Mata HP, Siegel EM, Vanderah TW, Porreca F, et al. The cannabinoid agonist WIN55,212-2 suppresses opioid-induced emesis in ferrets. Anesthesiology 2001;94:882–7.
Smith JE, Paton JF, Andrews PL. An arterially perfused decerebrate preparation of *Suncus murinus* (house musk shrew) for the study of emesis and swallowing. Exp Physiol 2002;87:563–74.
Smith JE, Paton JF, Andrews PL. Cardiorespiratory reflexes in a working heart-brainstem preparation of the house musk shrew *Suncus murinus*. Auton Neurosci 2001;89:54–9.
Thompson PI, Bingham S, Andrews PL, Patel N, Joel SP, Slevin ML. Morphine 6-glucuronide: a metabolite of morphine with greater emetic potency than morphine in the ferret. Br J Pharmacol 1992;106:3–8.
Torii Y, Mutoh M, Saito H, Matsuki N. Involvement of free radicals in cisplatin-induced emesis in *Suncus murinus*. Eur J Pharmacol 1993;248:131–5.
Torii Y, Saito H, Matsuki N. Induction of emesis in *Suncus murinus* by pyrogallol, a generator of free radicals. Br J Pharmacol 1994;111:431–4.
Torii Y, Saito H, Matsuki N. Selective blockade of cytotoxic drug-induced emesis by 5-HT3 receptor antagonists in *Suncus murinus*. Jpn J Pharmacol 1991;55:107–13.
Twycross R. The risks and benefits of corticosteroids in advanced cancer. Drug Saf 1994;11:163–78.
Ueno S, Matsuki N, Saito H. *Suncus murinus* as a new experimental model for motion sickness. Life Sci 1988;43:413–20.
Won MH, Matsuo K, Jo SM, Kang TC, Oh YS, Choi CD, et al. Brainstem origin of the efferent components of the cervical vagus nerve in the house musk shrew *Suncus murinus*. J Auton Nerv Syst 1998a;71:55–63.
Won MH, Matsuo K, Oh YS, Kitoh J. Brainstem topology of the vagal motoneurons projecting to the esophagus and stomach in the house musk shrew *Suncus murinus*. J Auton Nerv Syst 1998b;68:171–81.
Yamamoto K, Chan SW, Rudd JA, Lin G, Asano K, Yamatodani A. Involvement of hypothalamic glutamate in cisplatin-induced emesis in *Suncus murinus* (house musk shrew). J Pharmacol Sci 2009;109:631–4.
Yamamoto K, Ngan MP, Takeda N, Yamatodani A, Rudd JA. Differential activity of drugs to induce emesis and pica behavior in *Suncus murinus* (house musk shrew) and rats. Physiol Behav 2004;83:151–6.
Zhang C, Beckermann B, Kallifatidis G, Liu Z, Rittgen W, Edler L, et al. Corticosteroids induce chemotherapy resistance in the majority of tumour cells from bone, brain, breast, cervix, melanoma and neuroblastoma. Int J Oncol 2006a;29:1295–301.
Zhang C, Kolb A, Buchler P, Cato AC, Mattern J, Rittgen W, et al. Corticosteroid co-treatment induces resistance to chemotherapy in surgical resections, xenografts and established cell lines of pancreatic cancer. BMC Cancer 2006b;6:61.
Zhang Z. Iterative point matching for registration of free-form curves and surfaces. Int J Comput Vision 1994;13:119–52.

Please cite this article in press as: Huang D, et al. Computerized detection and analysis of cancer chemotherapy-induced emesis in a small animal model, musk shrew. J Neurosci Methods (2011), doi:10.1016/j.jneumeth.2011.02.032